Received: 19 May 2020 | Revised: 11 August 2020 | Accepted: 2 October 2020

DOI: 10.1002/tal.1812

RESEARCH ARTICLE

WILEY

Higher-mode buckling and friction in long and large-scale buckling-restrained braces

Ben Sitler | **Toru Takeuchi**

Department of Architecture and Building Engineering, Tokyo Institute of Technology, Tokyo, Japan

Correspondence
Ben Sitler, Department of Architecture and Building Engineering, Tokyo Institute of Technology, 4F-406, 2-12-1 Ookayama, Meguro-ku, Tokyo, Japan.
Email: sitler.b.aa@m.titech.ac.jp

Summary

Buckling-restrained braces (BRBs) are widely used as energy-dissipation members in seismic areas, and BRBs with 10–20 m workpoint lengths have been applied in practice, particularly in tall buildings and spatial structures. This paper investigates the adverse effects of the core yield length on the compressive overstrength factor, local compressive and tensile strains, and fatigue demands. Sets of 2D shell and 3D solid models were analyzed using Abaqus, considering core yield lengths of up to 14 m and LY100, LY225, SN400B, SN490B, SA440B, and SA700 steel grades. Higher-mode buckling and friction were shown to significantly amplify the compressive strain at the core ends and tensile strain at midspan, in part due to cyclic strain ratcheting, introducing the potential for core binding and premature necking. From these results, simple equations were proposed to calculate the compressive overstrength factor and to select the larger strong axis debonding gap and smaller design strain required for long BRBs.

KEYWORDS

buckling-restrained brace, core binding, friction, higher-mode buckling, long yield length, ultra low cycle fatigue

1 | INTRODUCTION

Tall buildings[1–3] and long-span spatial structures[4] (Figure 1a) in high seismic zones frequently employ buckling-restrained braces (BRBs) as seismic energy-dissipation devices. These applications typically require long BRBs with 10–20 m workpoint lengths (L_{wp}), which are difficult to test at full scale, while even longer BRBs have been employed as nominally elastic braces to limit the column and beam demands, rather than as primary energy-dissipation members.[5] Furthermore, rectangular cores (Figure 1b) are often used in lieu of built-up sections with welds along the core yield length (L_p) or tubular sections with inner faces unrestrained against local buckling, as these details significantly reduce the fatigue capacity. However, the weak axis radius of gyration is smaller in rectangular cores, which results in shorter plastic higher-mode buckling wavelengths and a greater number of contact points between the core and mortar during compressive cycles (Figure 1c). The small friction forces shed at the higher-mode buckling wavecrests accumulate to increase the total compressive force and local axial strain demands, which pose unique design challenges at the scale of long BRBs.

The most visible effect of friction in BRBs is to increase the compressive overstrength force (P_C), which exceeds the strain-hardened tensile force (P_T). These should be minimized, as the BRB overstrength forces control the design of the adjacent force-controlled elements (restrainer, connections and frame). P_T is a function of the yield force (P_Y) and strain hardening factor (ω) (Equation 1), while P_C also includes the compressive

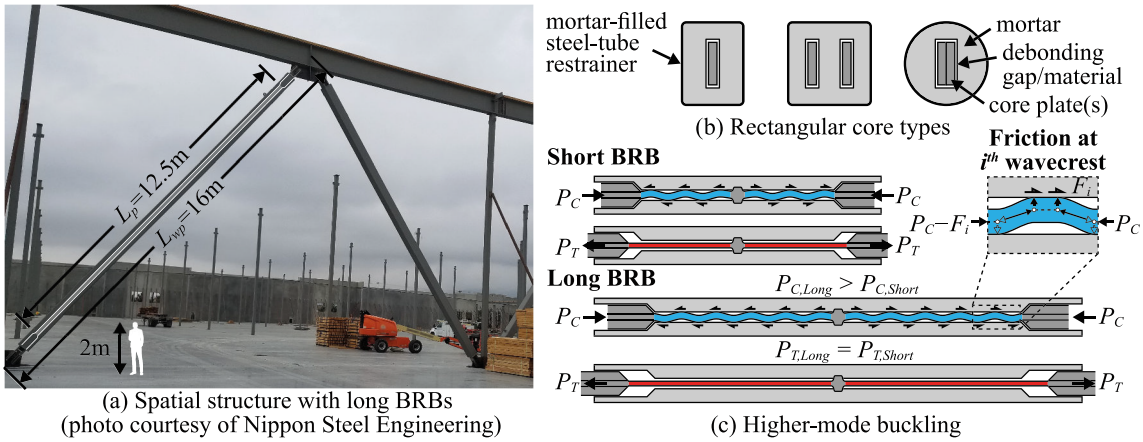

FIGURE 1 Friction in long, rectangular core buckling-restrained braces (BRBs)

overstrength factor (β) (Equation 2), which in a well-designed BRB consists of Poisson (β_P) (Equation 3) and friction components (β_F). While both β_P and β_F increase with the average axial strain ($\bar{\varepsilon}$) (Equation 4, where δ is the axial displacement), only β_F increases with the core yield length L_p.

$$\omega = \frac{P_T}{P_Y} \tag{1}$$

$$\beta = \frac{P_C}{P_T} = \beta_P \beta_F \tag{2}$$

$$\beta_P \approx 1 + 2 \cdot \bar{\varepsilon} \tag{3}$$

$$\bar{\varepsilon} = \frac{\delta}{L_p} \tag{4}$$

Current design standards[6] require that the compressive overstrength be confirmed through physical testing, but not necessarily using full-length specimens. Nevertheless, several test programs[7–9] have investigated the effect of the core thickness (t_c) and yield length (L_p) on β and have noted that the cumulative inelastic deformation (*CID*) at fracture decreases as the yield length and β increase. Figure 2a summarizes the key test results, indicating that for a given debonding interface, β_F approximately scales with the core's effective friction slenderness (λ_F) (Equation 5), which is proportional to the number of higher-mode buckling waves. Increasing β_F in turn reduces *CID*, which is adjusted in Figure 2b to a strain-consistent protocol using a Coffin-Manson exponent of m = 0.49.[10] These tests indicate that longer, thinner cores increase β_F and decrease *CID*. However, the effect is more pronounced for rectangular cores, as both β_F and *CID* are lower in compact, welded cruciform cores.

$$\lambda_F = \frac{L_F}{r_c} \tag{5}$$

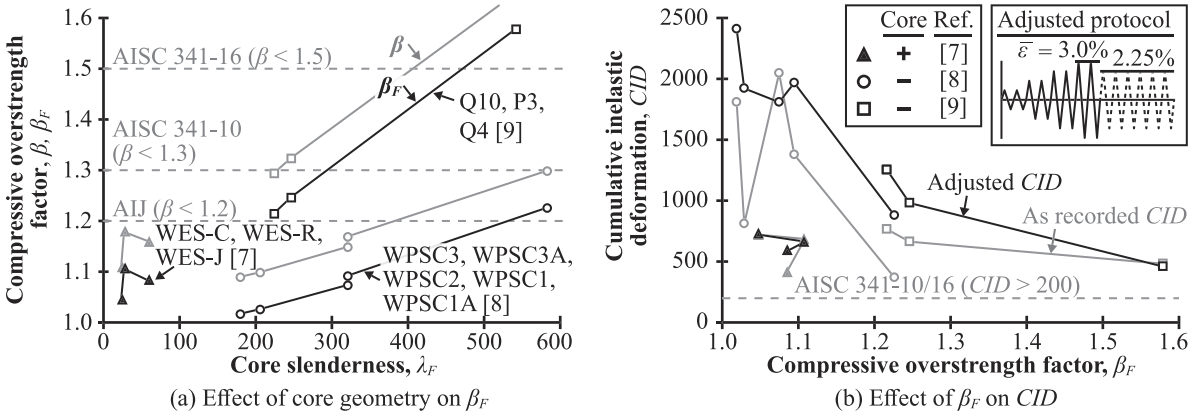

FIGURE 2 Long buckling-restrained brace (BRB) test results

where r_c is the core's minimum radius of gyration ($t_c/\sqrt{12}$ if rectangular) and L_F is the effective friction length ($L_p/2$ if a midspan shear key is present, or L_p if the restrainer is fixed to the core at one end).

Given that full-length testing is often impractical for long BRBs, analytical means to estimate these length effects are essential. Previous equations[7,11–13] to estimate β have utilized a single average wavelength and assumed that the friction force (F) accumulated along the effective friction length L_F is directly additive to the BRB compressive force (i.e., $|P_C| = \beta_P P_T + F$). Conversely, iterative numerical procedures,[14] finite element analyses,[7,14–16] and tests that directly monitored the local core demands[11,12,17] have observed significant variations in the wavelength, axial strain, and compressive force along the yield length. This suggests a more complex relationship between the friction and compressive forces and implies that the local axial strain demands may significantly deviate from $\pm\bar{\varepsilon}$. Furthermore, although these effects are likely sensitive to the shape of the stress–strain curve, previous investigations have been limited to a narrow range of mild steel grades similar to SN400B[11–13,15] and SN490B.[7,14,16,17] However, spatial structures and tall buildings regularly employ BRBs with significantly lower and higher steel grades to optimize the yield drift and/or core area.[4] The effect of steel grade on the compressive overstrength and axial strain has not yet been investigated, nor is it known if qualification tests, design methods, and specifications developed for short BRBs are directly applicable to long BRBs.

This paper numerically investigates the effects of the core dimensions and steel grade in long BRBs. First, the compressive overstrength and local axial strain demands are parametrically studied for a range of core properties using simplified 2D shell models. Next, the consequences of axial strain amplification in long BRBs, including core binding and premature necking, are analyzed using detailed 3D solid models. Finally, equations are proposed to evaluate and design for these effects.

2 | NUMERICAL MODEL (2D)

2.1 | Modeling assumptions

Although the axial response of most short BRBs simply mirrors the material hysteresis, higher-mode buckling introduces large local plastic strains, snap-through buckling, and sliding contact. Therefore, to improve the computational efficiency, the parametric study was conducted using Abaqus/Explicit[18] (quasi-static) and simplified 2D shell models that represent half the yield length of a rectangular core. These models capture the dominant higher-mode buckling action of the prototype BRB shown in Figure 3a, which features a competent midspan shear key and mortar-filled steel tube restrainer providing stiff, elastic confinement.

Each 2D model (Figure 3b) consisted of shell elements over a length $L_p/2$ and depth t_c. Based on a preliminary mesh sensitivity analysis, the core was subdivided into a fine mesh ($t_c/5 \times t_c/5$) of linear reduced integration plane stress elements (CPS4R). An analytical rigid surface was offset by the debonding gap thickness (s_w, per face) to represent the restrainer, with Coulomb friction (μ) assigned in the tangential direction and hard overclosure in the normal direction. Rotational restraint and half the brace displacements ($\pm\delta/2$) were applied at the free end to produce the same average axial strains $\bar{\varepsilon}$ as the full-length prototype BRB, while the far end was fixed but without constraining the transverse Poisson deformation. The core was modeled with a $0.5s_w$ sinusoidal initial imperfection, although the magnitude and shape of the imperfection were found to be uncorrelated with the plastic higher-mode buckling and friction response. Instead, the imperfection had the primary effect of initiating a different random nonlinear buckling path and shape.

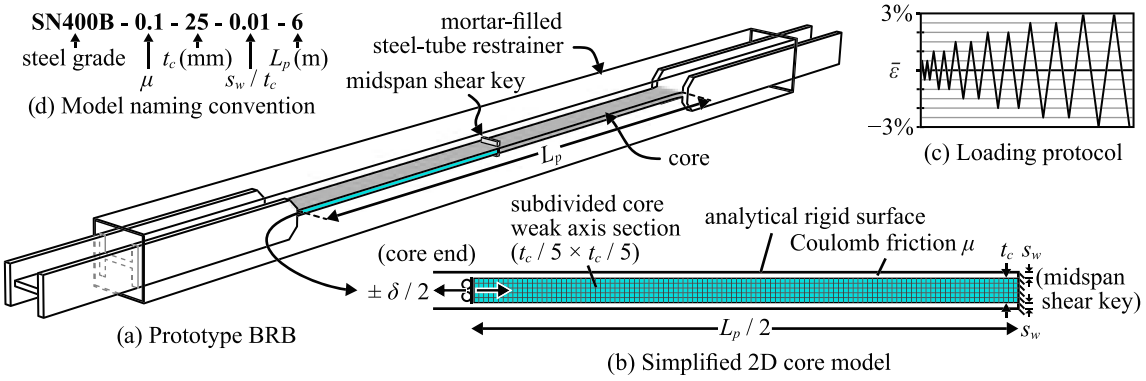

FIGURE 3 Finite element model (2D)

2.2 | Loading protocol

A gradually increasing, symmetric protocol was adopted (Figure 3c) that consisted of two cycles each at $\bar{\varepsilon}$ = 0.5%, 1.0%, 1.5%, 2.0%, 2.5%, and 3.0%. This was based on a protocol used to prequalify BRBs in Japan[4] but with 0.5% strain increments and no fatigue cycles. The compressive overstrength factor β was calculated from the peak tension and compression forces at the end of the second cycle at each amplitude.

2.3 | Model parameters

A range of core lengths (L_p = 2–14 m), thicknesses (t_c = 16–40 mm), and debonding gap ratios (s_w/t_c = 0.01–0.1) were considered, bounding typical values used in practice. Although there is currently little direct experimental data for real debonding interfaces, previous studies have adopted Coulomb friction coefficients between μ = 0.1–0.35[7,14,15] based on trial and error. Nevertheless, many common debonding materials exhibit pressure, velocity, slip distance, and temperature dependent friction coefficients or generate viscoelastic forces,[19] which may affect the axial force and strain distributions. However, these effects are highly supplier-specific and beyond the scope of the present study, which considered a Coulomb friction coefficient of μ = 0.1 or 0.3. The selected parameters are summarized in Table 1, with the 96 models per steel grade named according to the convention shown in Figure 3d.

2.4 | Constitutive steel material models

Although most BRBs employ LY225 (205 < f_y < 245 MPa), SN400B (235 < f_y < 355 MPa), SN490B (325 < f_y < 445 MPa), or equivalents (e.g., A36, A572-50), this study also considered LY100 (80 < f_y < 120 MPa), SA440B (440 < f_y < 540 MPa), and SA700 (700 < f_y < 900 MPa).[20] Low yield point grades (LY100, LY225) exhibit large monotonic ultimate strains (ε_u),[21] but significant isotropic hardening, which is particularly severe for LY100 and reduces the cyclic ultimate strain ($\varepsilon_u{}^{cyc}$).[22] Conversely, high strength grades (SA440B, SA700) exhibit negligible isotropic hardening, low ultimate strains ($\varepsilon_u{}^{cyc} \approx \varepsilon_u$ < 10%), and minimal overstrength ($f_y/f_u \approx$ 0.8–0.95).[21] These properties affect the shape of the stress–strain curves, with LY100 and LY225 featuring lower tangent stiffness than SN400B and SN490B, and the steep initial tangent stiffness of SA440B and SA700 rapidly decreasing as the limited overstrength saturates. Note that the effect of loading rate on the yield strength was not considered.

Abaqus' "combined hardening" model was calibrated to the coupon test data from Ono and Sato[21] (LY225∼SA700), Wang et al.[22] (LY100), and Yamazaki et al.,[23] targeting the tangent stiffness, cyclic stress, ultimate stress/strain, and strain ratcheting properties. This constitutive material model features a yield surface (σ_0) with isotropic hardening (Q_∞) that develops with the parameter b and cumulative plastic strain $\sum\varepsilon_p$, and kinematic hardening backstresses (α_i, where i = 1–3) that develop with the parameters C_i, γ_i and plastic strain magnitude ε_p. The true stress (σ^n) at the nth cycle is given by Equations 6a and 6b.

$$\sigma^n = \sigma_0 + Q_\infty\left(1 - e^{-b\cdot\sum^n \varepsilon_p}\right) + \sum \alpha_i^n \tag{6a}$$

$$\alpha_i^n = \frac{C_i}{\gamma_i} + \left(\alpha_i^{n-1} - \frac{C_i}{\gamma_i}\right) e^{-\gamma_i\left(\varepsilon_p^n - \varepsilon_p^{n-1}\right)} \tag{6b}$$

Additionally, the initial transient strain ratcheting increment ($\delta\varepsilon_{r,1}$) may be estimated by Equation 7, where σ_{Mean} is the mean true stress, $\Delta\varepsilon_p$ the averaged plastic strain range, and k = 2 the dominant non-saturated backstress after cycling at $\pm\varepsilon_p$. The strain ratcheting increment then asymptotically converges to the steady-state increment ($\delta\varepsilon_{r,\infty}$),[24] which is given by Equation 8.

TABLE 1 Model parameters

Steel grade		μ —	t_c mm	s_w/t_c —	L_p m
LY100	SN490B	0.1	16	0.01	2
LY225	SA440B	0.3	25	0.03	6
SN400B	SA700		40	0.05	10
				0.10	14

TABLE 2 Calibrated constitutive material model parameters

Steel grade	f_y^{EXP} MPa	E GPa	σ_0 MPa	C_1 MPa	γ_1 —	C_2 MPa	γ_2 —	C_3 MPa	γ_3 —	Q_∞ MPa	b —	f_u MPa	ε_u %	ε_u^{cyc} %
LY100	78	205	70	17,500	500	300	5	154	1	165	5	237	39	15
LY225	236	205	110	44,000	400	720	9	308	1	110	5	341	31	17
SN400B	259	205	130	52,500	350	2080	13	308	1	105	5	450	24	16
SN490B	342	205	200	46,400	290	2210	13	410	1	80	5	525	23	17
SA440B	505	205	300	67,500	270	3420	19	205	1	—	5	653	10	10
SA700	779	205	460	70,000	200	2470	19	205	1	—	5	856	7	7

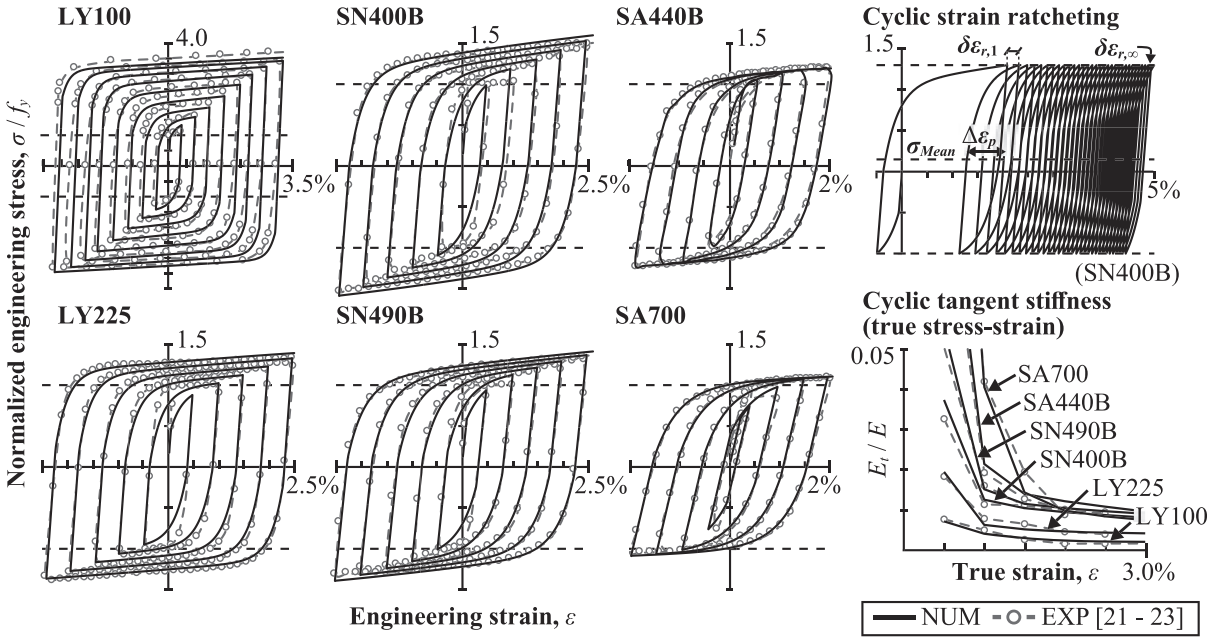

FIGURE 4 Constitutive material model calibration

$$\delta\varepsilon_{r,1} \approx 2\frac{\gamma_k}{C_k}\sigma_{Mean}\Delta\varepsilon_p \tag{7}$$

$$\delta\varepsilon_{r,\infty} = \frac{2\sigma_{Mean}}{\sum C_i \sinh(\gamma_i \Delta\varepsilon_p)} \tag{8}$$

Table 2 lists the experimental yield stress (f_y^{EXP}), calibrated parameters, and resulting ultimate stress and strains (f_u, ε_u, ε_u^{cyc}), while Figure 4 depicts example cyclic responses.

3 | NUMERICAL RESULTS (2D): COMPRESSIVE OVERSTRENGTH

The 2D parametric study results were used to establish the effects of the core geometry, friction, and steel grade on the compressive overstrength and axial strain, including the expected uncertainty.

3.1 | Effect of core yield length

A representative axial force-strain hysteresis is shown in Figure 5a for models with a large friction coefficient (μ = 0.3), a moderate debonding gap ratio (s_w/t_c = 0.03) and four different core yield lengths. Small drops in force were observed shortly after yielding in compression as the core

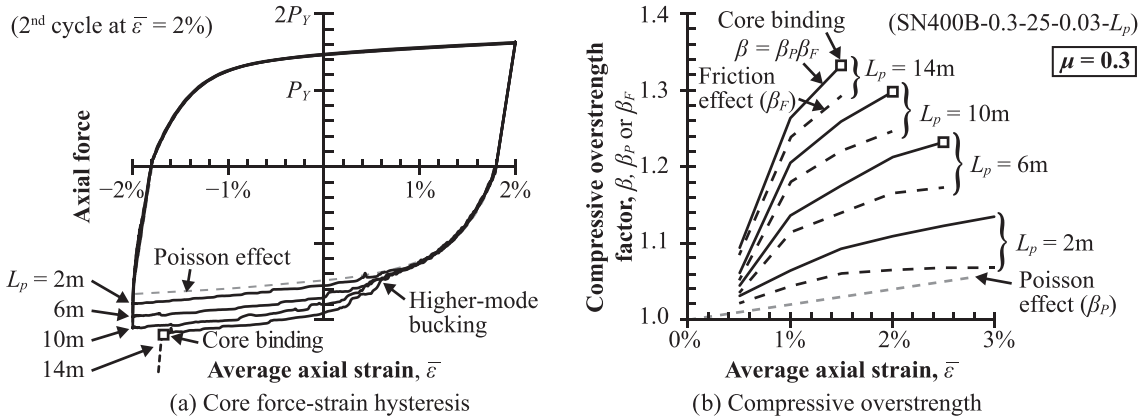

FIGURE 5 Effect of core yield length

started to buckle into progressively higher mode shapes. Friction between the core and mortar at the wavecrests then began to contribute to the compressive force, with the greater number of higher-mode buckling waves in the longer cores increasing the cumulative friction force.

The Poisson (β_P) and friction (β_F) contributions to the compressive overstrength β are shown in Figure 5b as a function of the average axial strain $\bar{\varepsilon}$. Note that β_P increased linearly with $\bar{\varepsilon}$, but β_F increased as a concave function of $\bar{\varepsilon}$. This was due to the shape of the stress–strain curve (Figure 4), as the rates of change in the stress, tangent stiffness, and higher-mode buckling wavelength decrease as $\bar{\varepsilon}$ increases, a trend that is reinforced by Poisson expansion, which reduces the total debonding gap and average higher-mode buckling waveheight by $-0.5t_c\,\bar{\varepsilon}$ Therefore, the rate of change in β_F decreases with increasing strain $\bar{\varepsilon}$.

However, there are some exceptions where the $\bar{\varepsilon}$-β plot may exhibit a non-convex "reverse S" shape. One such phenomena is core binding, which occurred in each of the longer models, and is where Poisson expansion exceeds the debonding gap, causing the core to wedge into the restrainer (refer to Section 6.1). The analysis was immediately terminated after detecting core binding in the 2D models, as only the isolated effect of higher-mode buckling and friction is of interest to this section.

The increase of β_F in long BRBs is fundamentally due to the greater number of higher-mode buckling waves, which is equal to the yield length divided by the average wavelength. Therefore, the average wavelength, or more specifically how the wavelength characteristics change in long BRBs, is also important to the analysis of length effects.

3.2 | Effect of higher-mode buckling wavelength

Each higher-mode buckling wavelength is composed of several parts: a flat wavecrest and two inclined sinusoidal bending segments that produce the lateral thrust and friction forces (Figure 6a). The sinusoidal segments may be estimated by equating the axial stress (σ) to the inelastic buckling stress and solving for the plastic wavelength (l_p).[4] As postulated by Shanley, upon formation of a new wave, the effective modulus (E_{eff}) gradually increases from the tangent modulus (E_t) as the convex face unloads but remains well below the reduced modulus (E_r) at the small amplitudes relevant to this problem. Upon contact, the new reaction and shear forces reduce the bending moment at the wavecrest, which Genna and Bregoli[25] found to increase the constrained effective length factor to k_e = 1.43–1.52 (k_e equals $2\beta\xi$ in Genna and Bregoli[25]). As additional compressive loading is applied, the wavecrest bending moment tends to zero, reducing E_{eff} to E_t, while increasing k_e to 2.0.[25] Nevertheless, these changes in E_{eff} and k_e approximately cancel out, making l_p a relatively stable material property. For a rectangular core with k_e = 2.0 and E_{eff} = E_t, the sinusoidal bending part of the weak axis wavelength ($l_{p,w}$) reduces to Equation 9 and is comparable to the average wavelength measured between the contact stress peaks of the 2D models, which are shown in Figure 6b. However, note that $l_{p,w}$ may vary along the yield length due to friction, and Equation 9 strictly only applies when contact occurs uniformly across the plate width, an effect that is discussed further in Section 7.1.

$$l_{p,w} = t_c \pi k_e \sqrt{\frac{E_{eff}}{3\sigma}}, \text{ where } k_e = 2.0 \text{ and } E_{eff} = E_t \tag{9}$$

Of greater interest to long BRBs is the wavecrest shape between the sinusoidal bending segments, which varies for each wavecrest along the core. After contact, the wavecrest flattens out (Figure 6a),[17] producing the same number of waves along the yield length even as the sinusoidal wavelength segments shorten until the wavecrest becomes long enough to accomodate a new wave. The increase from the sinusoidal to full wavelength is denoted the "wavecrest length factor" (ψ_W) and always starts as ψ_W = 1.0 upon formation of a new wave, which occurs via snap-

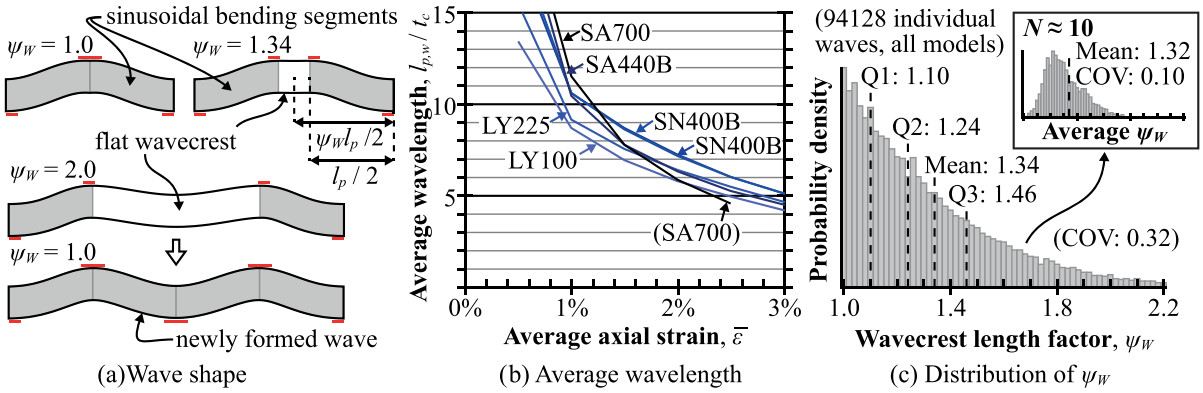

FIGURE 6 Higher-mode buckling wavelength

through buckling when a wavecrest exceeds $l_{p,w}$ (i.e., ψ_W = 2.0). Previous researchers have proposed deterministic values of ψ_W = 1.0[14] or 1.5[25] (ψ_W equals $\xi/2$ in these previous studies[14,25]). However, ψ_W is random and independent for individual waves at large strains when friction is included, and so a probabilistic estimate is preferred. Specifically, random variations in the initial imperfections lead to different nonlinear buckling paths with unique transient permutations in the number and shape of the waves. Given a fixed yield length L_p, more of the valid permutations will feature waves with small ψ_W values, skewing the distribution of ψ_W (Figure 6c).

Figure 6c shows the wavecrest length factors for the 94,128 individual waves from all models and strain levels, which followed a highly skewed distribution with a mean of $\psi_{W,mean}$ = 1.34 and a large coefficient of variation of $COV_{\psi W}$ = 0.32. Fortunately, the total number of waves and cumulative friction force depend on the average ψ_W of the N wavecrests along the friction length. From the Central Limit Theorem, the distribution of the average ψ_W becomes normal as N increases, while the coefficient of variation decreases by $1/\sqrt{N}$. For example, models with $N \approx 10$ wavecrests still had a mean of ψ_W = 1.32, but the coefficient of variation reduced to 0.10, and then to 0.04 for $N \approx 100$. Therefore, the uncertainty in the number of waves due to the random wavecrest variation reduces in long BRBs. However, β_F simultaneously increases with the number of wavecrests N in long BRBs, and so the standard deviation of β_F (Equation 10) remains relatively stable, increasing only slightly from $SD_{\beta F}$ = 0.015 to 0.025 as μ, s_w and N increase. For simplicity, $SD_{\beta F} \approx 0.02$ may be assumed for both short and long BRBs.

$$SD_{\beta_F} = \frac{COV_{\psi_\omega}}{\sqrt{N}}(\beta_F - 1) \approx 0.02 \tag{10}$$

3.3 | Implications for scaling β_F to a long BRB

This "wavecrest length uncertainty" may be observed in the numerical results, as Figure 7a indicates that β_F scaled linearly with μ, s_w/t_c, and L_p/t_c, on average, while exhibiting a uniform scatter of $\beta_F \pm 0.02$. Note that this intrinsic uncertainty is additive to the experimental error and affects both numerical and experimental studies. Therefore, significant error may result when extrapolating β_F from a single specimen, as indicated by Figure 7b, where β_{F0} is the friction overstrength of the shorter or lower friction reference specimen. Linear scale factors (SF) from $1.4 < SF < 5$ were considered by varying either μ, s_w/t_c, L_p, or t_c. The uncertainty in β_{F0} was amplified by scaling and produced particularly large errors for $SF > 2.0$. For example, 12% of the pairs with $SF > 2.0$ underestimated the compressive force in the extrapolated model by 5–10%, while another 5% underestimated the compressive force by 10–15%. Whether this is of engineering significance depends on the safety margin of the adjacent force-controlled elements.

In summary, it appears that β_F is only linearly proportional to the yield length L_p in an average sense, and even "perfect" BRBs are subjected to a standard deviation of about $\beta_F \pm 0.02$, regardless of length. This inherent uncertainty in the wavecrest length makes scaling β_F from a single specimen inadvisable. While full-length testing is always preferred, potential solutions to mitigate the scaling error may be to test multiple identical short specimens (reducing the uncertainty in β_{F0}), limit the permissible scale factor (e.g., yield lengths no longer than $1.5L_p$, given the same debonding gap and core thickness), or calibrate an analytical model (as presented in Section 7) against a large test catalog.

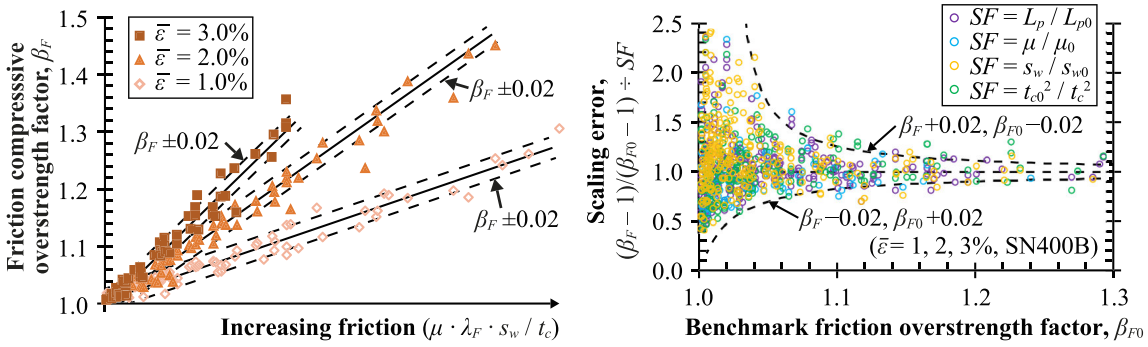

(a) Compressive overstrength and friction (b) Scaling error

FIGURE 7 Effect of wavecrest length uncertainty

3.4 | Effect of steel grade

The steel grade may also affect β_F, as Equation 9 indicates that the wavelength is a function of the ratio of the tangent stiffness to axial stress, which varies with the kinematic and isotropic hardening characteristics. This effect may be particularly pronounced for long BRBs in tall buildings and spatial structures using atypical materials, such as LY100, SA440B, and SA700. This was investigated by comparing β_F for the different steel grades to the corresponding SN400B models.

Figure 8a depicts the mean and mean ± standard deviation of β_F collated from the model-by-model comparisons to SN400B. While the SN490B models exhibited nearly identical behavior to the SN400B models, the other steel grades each produced a higher β_F. The large ultimate strains (and isotropic hardening for LY100) of the low yield steels resulted in low tangent stiffness and short wavelengths. This increased the quantity (β_F − 1) by +150% (LY100) and +50% (LY225) compared to SN400B, gradually converging to increases of +50% (LY100) and +20% (LY225) for $\bar{\varepsilon}$ > 2%. The difference in β_F also closely matched the difference in tangent stiffness for the high strength steels, as the steep kinematic hardening and longer wavelengths at small strains initially reduced β_F, but kinematic hardening rapidly saturated and so the quantity (β_F − 1) increased by +20% (SA440B) and +50% (SA700) at $\bar{\varepsilon}$ = 1.5%.

However, the increase in β_F for the atypical steel grades did not necessarily increase the combined compressive overstrength ($\beta\omega$), which is the actual overstrength used to design the force-controlled elements. Figure 8b shows the change in $\beta\omega$ for a model that achieved β = 1.3 at $\bar{\varepsilon}$ = 3.0% for SN400B. The severe isotropic strain hardening of LY100 was aggravated by the already high β_F, while the increase in β_F was fully offset by reduced strain hardening for the high strength steels. Therefore, even though β_F increased as the steel grade deviated from SN400B, only the low yield point steels were penalized in terms of $\beta\omega$. Nevertheless, there is a risk that engineers may attempt to adjust ω using short test specimens, but then extrapolate β_F using specimens with a different steel grade, which may significantly underestimate $\beta\omega$.

In summary, there was negligible difference in β_F between SN400B and SN490B, and the relative performance of the other steel grades was dominated by the difference in tangent stiffness. Additionally, β_F increased for both the significantly higher (e.g., SA440B and SA700) and lower (e.g., LY100, LY225) steel grades, and so design standards may consider limiting the applicability of test specimens by yield stress (e.g., 0.7–1.4f_y, where f_y is the test yield stress). For high strength steels, it may be prudent to adopt a smaller design strain (e.g., $\bar{\varepsilon}$ < 2%), as β_F increased rapidly at

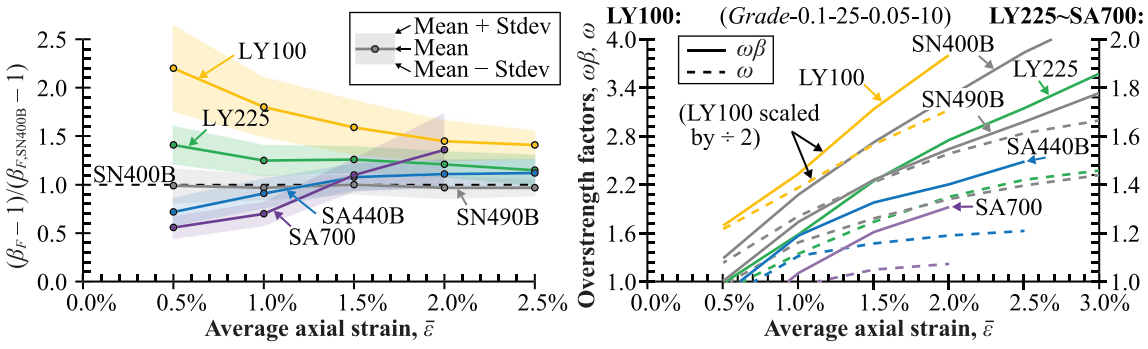

(a) Friction compressive overstrength (b) Total compressive overstrength

FIGURE 8 Effect of steel grade on β_F and $\beta\omega$

large strains. Finally, the severe isotropic hardening of LY100 was compounded by low tangent stiffness, which amplified β_F. Low yield point steels with similar characteristics may be less suitable for long BRBs, or at the least demand full-length testing.

4 | NUMERICAL RESULTS (2D): AXIAL STRAIN AMPLIFICATION

Although β_F is primary used to determine the compressive force, substantial reductions in the fatigue capacity have been observed in BRBs with high compressive overstrength factors (Figure 2b), which suggests that β_F may significantly affect the strain demands. This section reviews the mechanics of higher-mode buckling in BRBs and proposes empirical axial strain amplification factors derived from the 2D results.

4.1 | Axial distribution of force and strain

During compression cycles, friction at the higher-mode buckling wavecrests gradually sheds force to the restrainer, such that the core compressive force reaches a minimum at the fixity point (e.g., midspan shear key) (Figure 9). According to the constitutive relationship defined by the cyclic stress–strain curve, the axial strains also decrease along the core, potentially resulting in permanent tensile strains at midspan if β_F is large. Additionally, displacement compatibility requires that the axial strains $\varepsilon(x)$ integrated along the full core yield length from $x = 0$ to L_p equal the prescribed displacement (δ) (Equation 11), assuming that the higher-mode buckling amplitude is small and the elastic connection deformations are negligible.

$$\delta = \bar{\varepsilon} \cdot L_p = \int_0^{L_p} \varepsilon(x) \cdot dx \tag{11}$$

This implies that the local axial strain only equals the average axial strain $\bar{\varepsilon}$ at the balance point(s) shown in Figure 9. Figure 10a shows that the balance point position (x_{bal}) starts at $0.5L_F$ (e.g., at the quarterpoints if a midspan shear key is present) and then gradually moves toward the free ends as β_F increases, which produces an increasingly nonlinear strain distribution with larger compressive strains at the core ends (ε_C). As the balance point approximately cycles symmetrically from $\pm\bar{\varepsilon}$ (i.e., ε (x_{bal}) = $\pm\bar{\varepsilon}$), the core force at x_{bal} equals the frictionless case (i.e., P (x_{bal}) = $-\beta_P P_T$, + P_T), while the increase in the BRB compressive force equals the friction force accumulated from $x = 0$ to x_{bal}. This is a key point, as it implies that the axial force transferred to the restrainer from x = 0 to L_F may significantly exceed the observed increase in the BRB compressive force. Although the axial force distribution is slightly nonlinear,[11] the increase in compressive force was only 50% to 65% of the total friction force (F) accumulated along L_F (Figure 10b). This may be approximated as an overstrength-to-friction force ratio of $\rho \approx 55\%$ (Equation 12) for $\beta_F < 1.4$.

$$\rho = \frac{(\beta_F - 1)\beta_P P_T}{F} \approx 0.55 \tag{12}$$

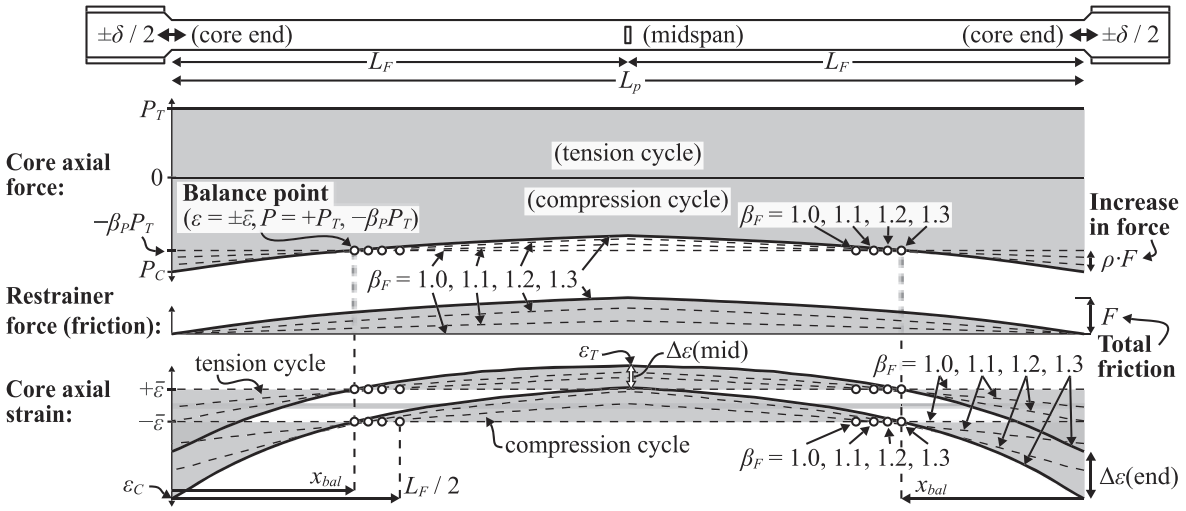

FIGURE 9 Average axial force and strain distribution

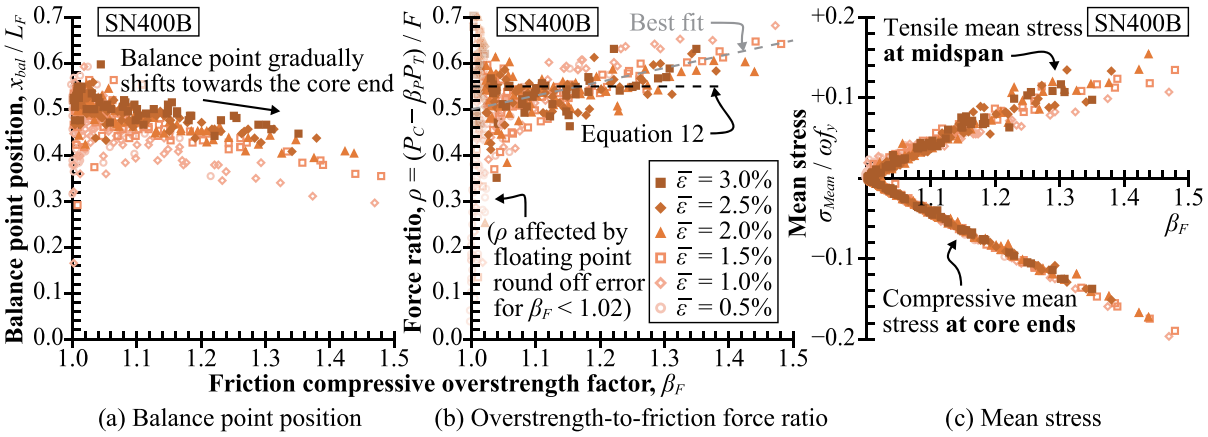

FIGURE 10 Friction force and mean stress

The axial strains are further amplified by the large mean forces that develop with an increasing β_F (Figure 10c), as equilibrium requires the core ends to cycle between P_c (= $-\beta_F\beta_P P_T$) and P_T, and the core midspan to cycle between $P_c - F$ (<$-\beta_P P_T$) and P_T. Non-zero mean stresses drive cyclic strain ratcheting,[24] a phenomenon where strains increase in the direction of the mean stress when cycled between constant, but unequal stresses. Strain ratcheting is particularly severe when the strain range is large, as is the case for BRBs, and ratcheting accelerates in tension (but not in compression) when cycling between forces, rather than true stresses, as Poisson contraction progressively increases the true tensile stress (and strain increment) required to maintain the constant prescribed force.

4.2 | Compressive strain amplification

The friction and cyclic strain amplifications produced large compressive strains (ε_C) at the core ends, and Figure 11 shows that the normalized compressive strain amplification ($\varepsilon_C/\bar{\varepsilon}$) increases with β_F. Although the amplification depends on the loading history and susceptibility to cyclic strain ratcheting, the regressions provided in Equation 13 indicate that ε_C is a net linear function of $\bar{\varepsilon}$ and β_F. From Equation 7, the susceptibility to strain ratcheting for a small number of cycles depends on kinematic hardening in the intermediate strain range, which is minimized for SN400B and SN490B. Consequently, these mild steels once again exhibited the best performance, while greater strain amplification was observed for both the low yield (LY225 + 5%, LY100 + 25%), and high strength (SA440 + 50%, SA700 + 90%) steel grades, compounding the higher β_F values expected for these materials.

$$\frac{\varepsilon_C}{\bar{\varepsilon}} \approx \begin{cases} 1+19(\beta_F-1) & \text{LY100} \\ 1+16(\beta_F-1) & \text{LY225} \\ 1+15(\beta_F-1) & \text{SN400B} \\ 1+15(\beta_F-1) & \text{SN490B} \\ 1+22(\beta_F-1) & \text{SA440B} \\ 1+28(\beta_F-1) & \text{SA700} \end{cases} \tag{13}$$

4.3 | Tensile strain amplification

The tensile strains at midspan (ε_T) were initially amplified less than in compression due to the partial strain recovery associated with the exponential axial strain distribution (Figure 9). However, the amplification factors ($\varepsilon_T/\bar{\varepsilon}$) shown in Figure 12 increased with both the mean stress (proportional to β_F) and strain range (proportional to $\bar{\varepsilon}$) due to cyclic strain ratcheting, which as discussed earlier, is more critical for mean tension forces. The regressions in Equation 14 indicate that $\varepsilon_T/\bar{\varepsilon}$ was a nonlinear function of $\bar{\varepsilon}$ and equality with the compressive strain amplification factors was only reached at $\bar{\varepsilon}$ = 2.2% to 3.4%, depending on the steel grade. Once again, SA700 performed poorly, as this was the only material with a cyclic ultimate strain (ε_u^{cyc}) of less than 10%. Few of the SA700 models completed the full protocol as the analysis was terminated if concentrated

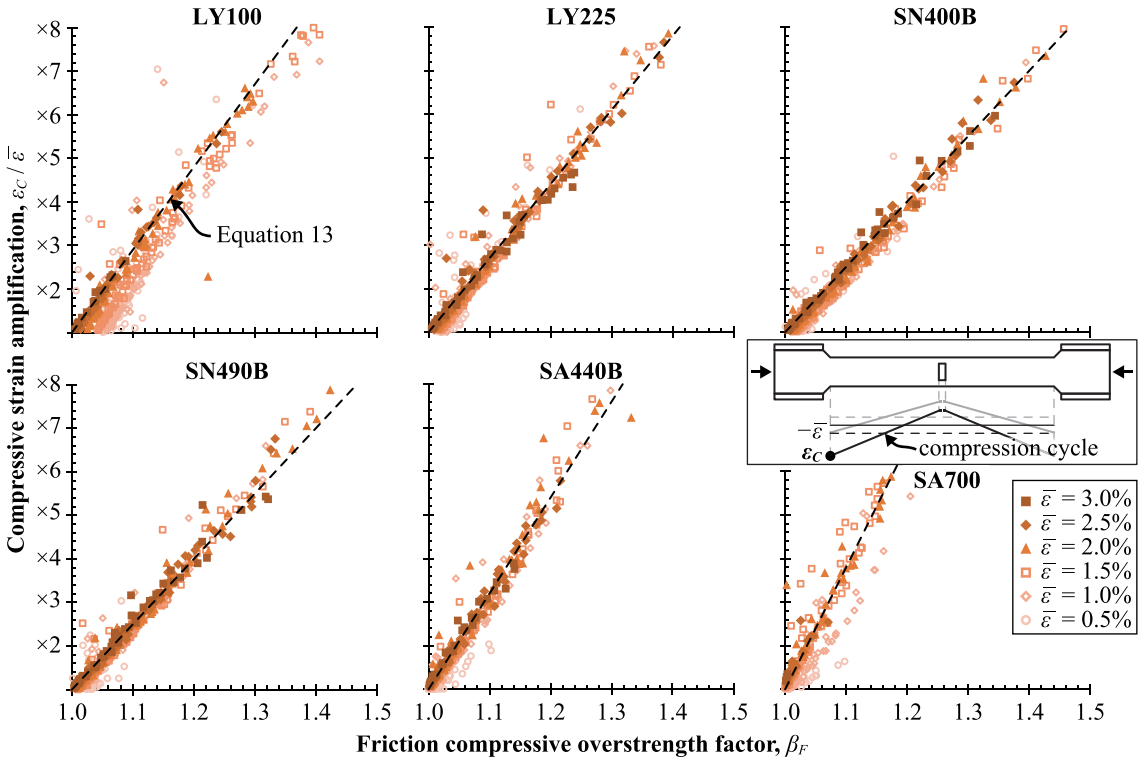

FIGURE 11 Compressive strain amplification at core ends

necking or core binding was detected, resulting in insufficient data at large strains for a regression. Similarly, despite the large monotonic ultimate strain of LY100, concentrated necking frequently occurred due to the reduced cyclic ultimate strain caused by isotropic hardening and the compounding effects of β_F and $\varepsilon_T/\bar{\varepsilon}$.

$$\frac{\varepsilon_T}{\bar{\varepsilon}} \approx \begin{cases} 1+19\left(0.30-8.7\cdot\bar{\varepsilon}+1900\cdot\bar{\varepsilon}^2\right)\left(\beta_F-1\right) & \text{LY100}\ (\varepsilon_T=|\varepsilon_C|\ \text{at}\ \bar{\varepsilon}=2.2\%) \\ 1+16\left(0.24-3.5\cdot\bar{\varepsilon}+1040\cdot\bar{\varepsilon}^2\right)\left(\beta_F-1\right) & \text{LY225}\ (\varepsilon_T=|\varepsilon_C|\ \text{at}\ \bar{\varepsilon}=2.9\%) \\ 1+15\left(0.18-3.1\cdot\bar{\varepsilon}+780\cdot\bar{\varepsilon}^2\right)\left(\beta_F-1\right) & \text{SN400B}\ (\varepsilon_T=|\varepsilon_C|\ \text{at}\ \bar{\varepsilon}=3.4\%) \\ 1+15\left(0.18-9.0\cdot\bar{\varepsilon}+1000\cdot\bar{\varepsilon}^2\right)\left(\beta_F-1\right) & \text{SN490B}\ (\varepsilon_T=|\varepsilon_C|\ \text{at}\ \bar{\varepsilon}=3.3\%) \\ 1+22\left(0.18-20\cdot\bar{\varepsilon}+1600\cdot\bar{\varepsilon}^2\right)\left(\beta_F-1\right) & \text{SA440B}\ (\varepsilon_T=|\varepsilon_C|\ \text{at}\ \bar{\varepsilon}=3.0\%) \end{cases} \tag{14}$$

4.4 | Strain range amplification

Although the peak compressive and tensile strain amplitudes increased with β_F (Figures 11 and 12), these peak strains did not occur at the same location. The axial strain ranges at the core end ($\Delta\varepsilon$ (end)) and midspan ($\Delta\varepsilon$ (mid)) are shown in Figure 13 for SN400B, and only slightly deviated from the average axial strain range ($2\bar{\varepsilon}$) defined by the loading protocol.

The strain range at the core ends increased with β_F, while the strain range at midspan decreased with increasing β_F, and the strains along the entire core converged toward $2\bar{\varepsilon}$ as the applied strain increased. Thus, the trend was for the strain range amplification to oppose the amplification of the tensile strain amplitude, slightly mitigating the detrimental effect of β_F on the fatigue capacity. Crucially, this implies that the reduction in *CID* will generally be less than the increase in yield length and β_F. Although only the results for SN400B are shown in Figure 13, the other steel grades exhibited similar behavior, with the strain range increasing at the core ends, reducing at midspan, and converging toward $2\bar{\varepsilon}$.

Nevertheless, there are several limitations to this analysis. First, the strains in Figures 11–13 refer solely to the section-averaged axial strains, and do not include bending strains introduced by higher-mode buckling, nor strain concentrations due to fabrication imperfections and changes in

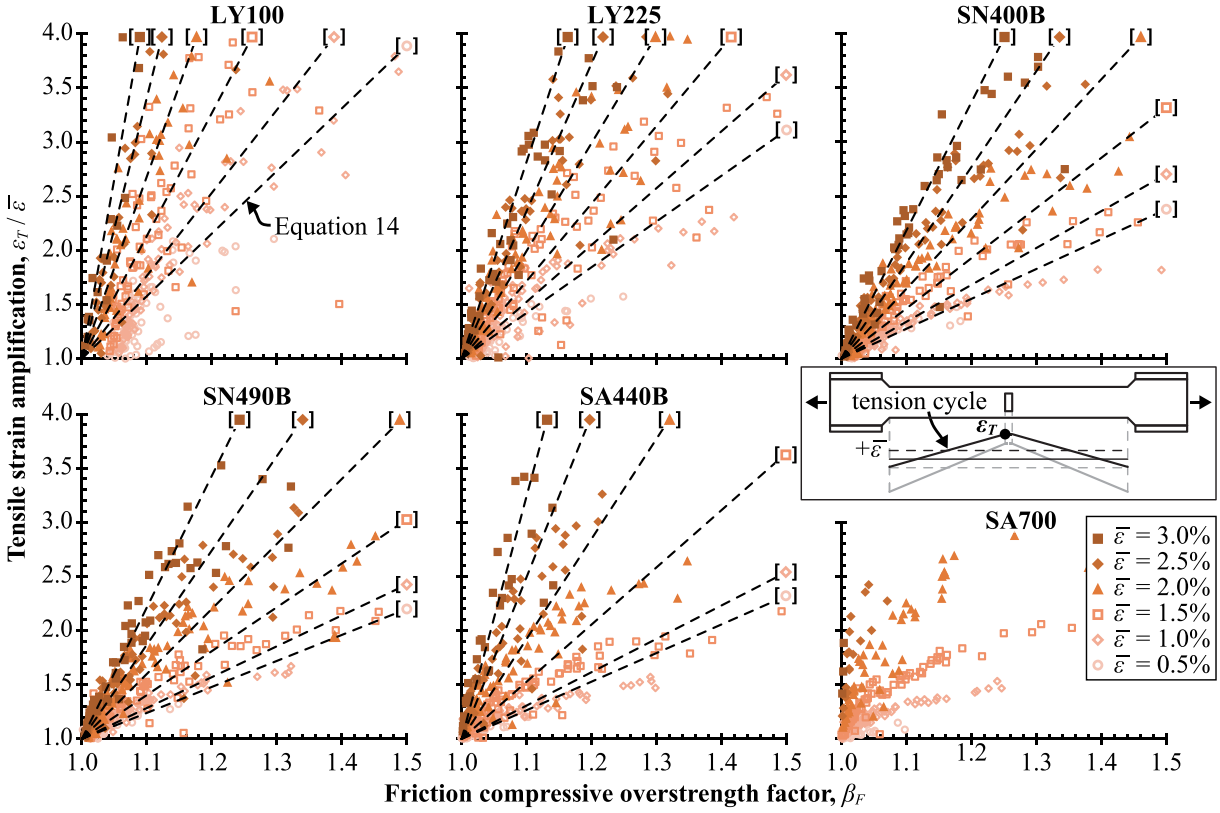

FIGURE 12 Tensile strain amplification at midspan

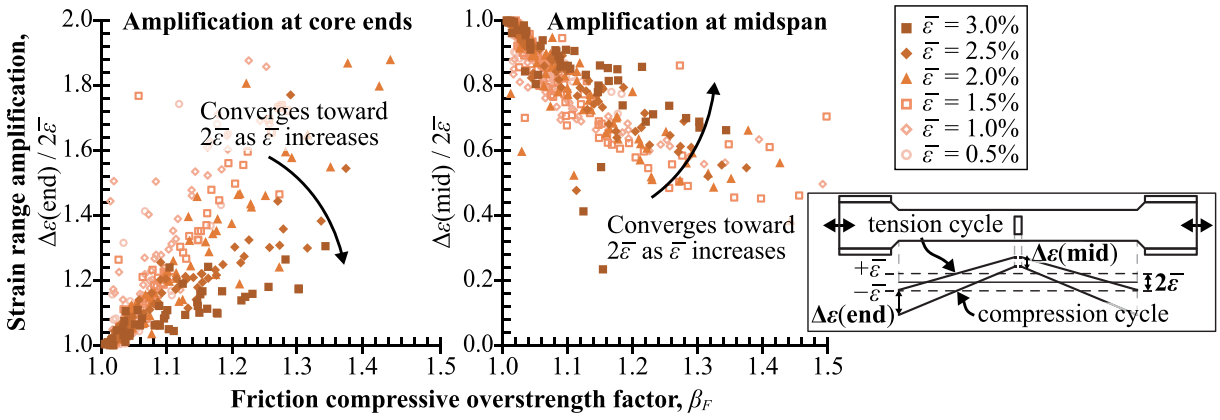

FIGURE 13 Cyclic strain range amplification

cross section. Also, the compressive and tensile strain amplifications are strictly only valid for the loading protocol in Figure 3c, as a significant component is due to cyclic strain ratcheting. Additional runs were conducted using the decreasing and asymmetric loading protocols from Wu et al.,[16] which were found to produce either higher or lower transient amplification factors (due to space the plots are not presented here). However, the amplification factors converged to Equations 13 and 14 as the protocol reverted to constant or ascending cycles. Additionally, the maximum compressive and tensile strains were always less than those obtained from a symmetric, gradually increasing protocol with equal maximum amplitude, suggesting that Equations 13 and 14 are conservative. Also, the strain amplifications defined by Equations 13 and 14 are specific to the material calibrations in Table 2, but other steel grades should follow the same trends.

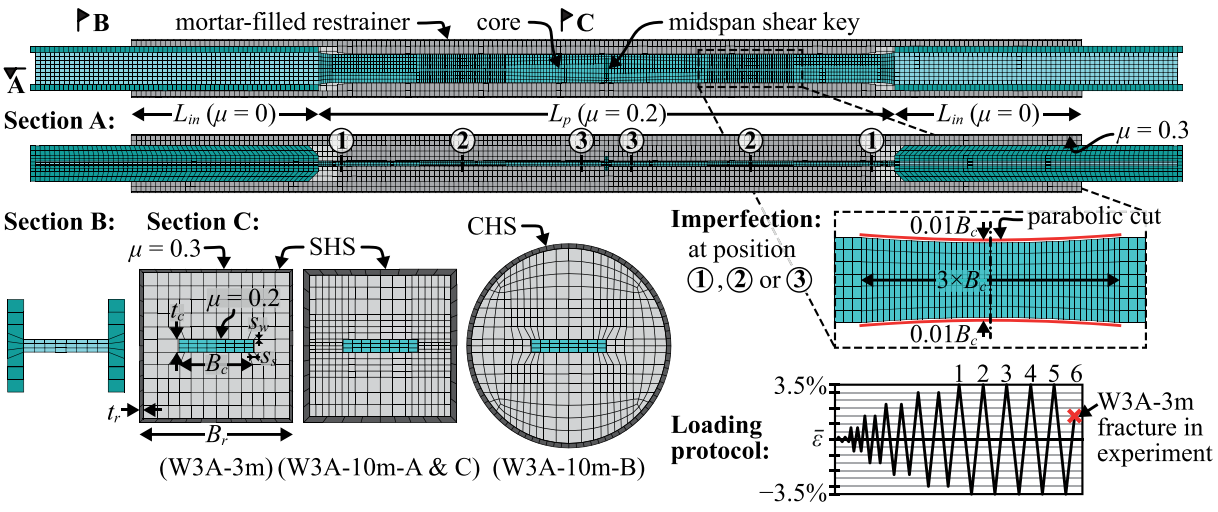

FIGURE 14 Finite element model (3D)

5 | NUMERICAL MODEL (3D)

5.1 | Modeling assumptions

Given the significant friction-induced strain amplification expected in long BRBs, detailed 3D models (Figure 14) were analyzed to investigate the consequences of large local compressive and tensile strains. Weak (s_w) and strong (s_s) axis debonding gaps were provided at each face in the core thickness (t_c) and width (B_c) directions, and general contact with Coulomb friction and hard contact was assigned at the restrainer-mortar (μ = 0.3) and core-mortar (μ = 0.2) interfaces but with μ = 0.0 along the insert length. The mortar was modeled using "concrete damaged plasticity" following Nguyen and Whittaker[26] (Popovics/Saenz compressive stress–strain with f_{ck} = 45 MPa at ε_c = 0.24%, compression damage d_c = 0.3, and Cornellissen tensile stress-crack width with f_t = 3.8 MPa and fracture energy G_f = 53 N/m) but with a lower dilation angle of 20° to limit volumetric expansion. Note that this neglects the increased ductility of confined concrete. A coarser mesh (t_c/3 thickness × t_c/2 breadth × t_c length) of linear reduced-integration elements (C3D8R) with relaxed stiffness hourglass control was adopted to improve runtime, at a small cost in accuracy. No initial imperfection offset was assigned, as the intent was not to model global buckling, and as discussed previously, imperfections are uncorrelated with the plastic higher-mode buckling and friction response.

5.2 | Model summary and loading protocol

Specimen WPSC3A from Terashima[8] was adopted as a benchmark, but is referred to as W3A-3m in this paper. This specimen featured a rectangular core ($B_c \times t_c$ = 148 × 25 mm, L_p = 3.0 m) with a midspan shear key, square hollow section (SHS) restrainer ($B_r \times t_r$ = 305 × 6.4 mm) and welded connections with long insert lengths (L_{in} = 975 mm). The other dimensions follow Terashima,[8] except that the A36 core was modeled using the SN400B material from Table 2. The subassemblage protocol used in the test (Figure 14) consisted of 2 cycles each at $\bar{\varepsilon}$ = 0.15%, 0.75%, 1.5%, 2.25%, 3.0%, and 3.5%, with fatigue cycles at $\bar{\varepsilon}$ = 3.5% continued until fracture and equal displacements applied in the transverse "in-frame" direction, which generated subassemblage rotations due to end rotational restraints.

The primary purpose of applying subassemblage rotations was to induce bending strains at the core ends, but these may also introduce connection friction forces, depending on the connection geometry and insert length. The long insert length and a friction coefficient of μ = 0.2 was estimated to produce connection friction forces of about ±4%P_T, with equal forces generated in the tension and compression half-cycles. However, the connection friction forces did not affect the compressive overstrength factor nor friction-induced strain amplification, and so the insert lengths were assigned frictionless contact (μ = 0) for simplicity.

Long BRBs (Table 3) were then modeled with a L_p = 10 m yield length and thicker (t_r = 12 mm) SHS restrainer (W3A-10m-A). Minor modifications were investigated, including a circular hollow section (CHS) restrainer for W3A-10m-B and thicker strong axis debonding gap (s_s/B_c = 0.02) for W3A-10m-C. W3A-3m and W3A-10m-C were also analyzed with local 2% reductions in the core width at the ① core ends, ② quarter-points, or ③ midspan to represent fabrication imperfections. However, the shorter benchmark specimen (W3A-3m) still qualifies all four designs under the similitude rules of AISC 341-16 (§K3.3c),[6] as the buckling safety factor, connection details, core shape and orientation, yield force, restrainer composition, and debonding material are not changed.

TABLE 3 Model summary

Model	L_p	Restrainer	s_w/t_c	s_s/B_c	Imperfection	Limit state ($\bar{\varepsilon}$)	β at $\bar{\varepsilon}$= 2.25%	β at $\bar{\varepsilon}$= 3.5%
W3A-3m	3 m	SHS 305 × 6.4	0.04	0.01	–, ①, ②, or ③	Fatigue (6 × 3.5%)	1.07	1.12
W3A-10m-A	10 m	SHS 305 × 12	0.04	0.01	–	Binding (2.25%)	1.16	1.41
W3A-10m-B	10 m	CHS 406 × 9	0.04	0.01	–	Binding (2.25%)	1.18	>2.03
W3A-10m-C	10 m	SHS 305 × 12	0.04	0.02	–, ①, ②, or ③	Fatigue (3 × 3.5%)	1.14	1.23

5.3 | Fatigue and core binding limits

Strain amplification is a concern for long BRBs, as it may cause core binding at the core ends or earlier fracture at midspan. Core binding occurs when the lateral Poisson expansion associated with the compressive strain exceeds the effective debonding gap, which causes the core to wedge into the confining mortar and transmit large forces to the restrainer. The critical binding strain (ε_{bind}) may be estimated by Equation 15, assuming a plastic Poisson ratio of 0.5 and nearly crushed mortar.

$$\varepsilon_{bind} = \min\left\{\frac{2(s_w + t_{m,w}\varepsilon_{cu})}{0.5t_c}, \frac{2(s_s + t_{m,s}\varepsilon_{cu})}{0.5B_c}\right\} \tag{15}$$

where s_w and s_s are the as-built debonding gaps per face, $t_{m,w}$ and $t_{m,s}$ are the mortar thicknesses per side (e.g., $t_{m,w} = (B_r - 2t_r - B_c)/2$), and $\varepsilon_{cu} \approx 0.25\%$ is the mortar strain at the peak unconfined strength.

The fatigue capacity was evaluated using the stress weighed damage model (*SWDM*),[27] an ultra low cycle fatigue (*ULCF*) model developed for the low triaxiality conditions typical of BRBs that considers the incremental equivalent plastic strain (ε_p), triaxiality (T), and lode angle parameter (ξ). Crack propagation was not directly modeled, as necking or tearing along the yield length was assumed to result in gross section fracture within a single cycle. This is a reasonable assumption given that BRB cores are subjected to direct tension and are relatively long, which promotes rapid crack propagation. Additionally, although fatigue analysis has considerable uncertainty and probabilistic methods are available,[8] the relative performance of long BRBs was estimated by assuming that fracture occurs when the void growth index (*VGI*) exceeds the critical cyclic void growth index (VGI^{cr}_{cyc}) (Equations 16a and 16b). Material properties calibrated for A36[8] were adopted, with $\lambda = 0.22$ and $VGI^{cr}_{mono} = 1.28$ at the flame-cut edges and weld heat-affected zones, and $VGI^{cr}_{mono} = 7.06$ elsewhere. Note that Terashima[8] originally calibrated this model for BRBs and investigated fatigue and fracture in the absence of significant friction effects; this study is distinguished by considering friction-induced strain amplification.

$$VGI = \int \left(1.3e^{1.3T} - e^{-1.3T}\right)e^{0.33|\xi|}d\varepsilon_p \geq 0 \tag{16a}$$

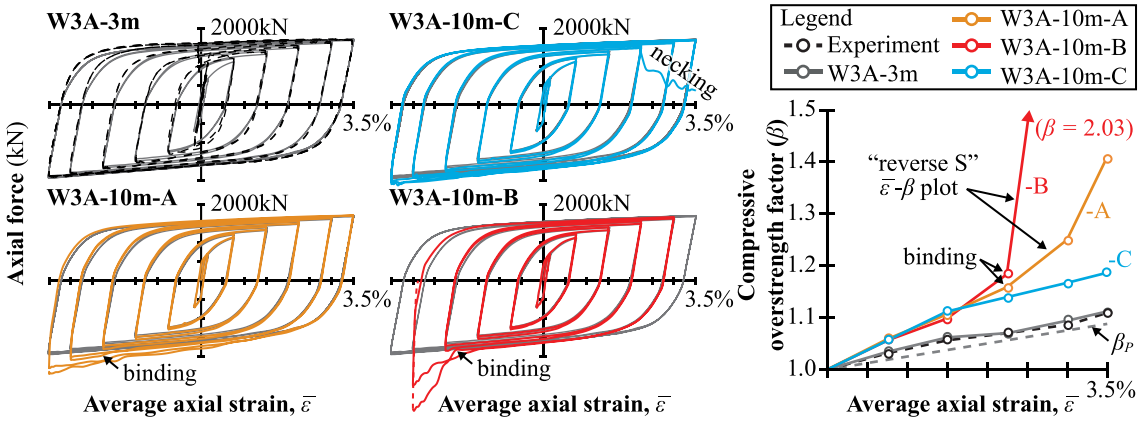

FIGURE 15 Axial hysteresis and compressive overstrength

$$VGI_{cyc}^{cr} = \frac{e^{\lambda \sum \varepsilon_p}}{VGI_{mono}^{cr}} \quad (16b)$$

6 | NUMERICAL RESULTS (3D)

6.1 | Friction-induced core binding

The axial hysteresis and compressive overstrength are shown in Figure 15, with W3A-3m exhibiting excellent agreement with the experimental results, achieving β = 1.07 at $\bar{\varepsilon}$ = 2.25% (i.e., β_F = 1.02) and β = 1.12 at $\bar{\varepsilon}$ = 3.5% (i.e., β_F = 1.04), as compared to β = 1.07 and β = 1.11 in the experiment. Core binding did not occur for W3A-3m in the finite element analysis nor experiment. Although the W3A-3m, W3A-10m-A, and W3A-10m-B models all featured the same strong-axis debonding gap (s_s/B_c = 0.01, ε_{bind} = 5%), both 10 m models started to experience core binding during the second cycle at $\bar{\varepsilon}$ = 2.25%, with the core end compressive strains exceeding 5% and β equal to 1.16 (W3A-10m-A) and 1.18 (W3A-10m-A).

After core binding initiated, β increased to 1.25 at $\bar{\varepsilon}$ = 3.0% and 1.41 at $\bar{\varepsilon}$ = 3.5% for W3A-10m-A, while β increased to 2.03 at $\bar{\varepsilon}$ = 3.0% for W3A-10m-B, at which point the analysis was terminated. These sharp increases produced a non-convex "reverse *S*" shaped plot of $\bar{\varepsilon}$ versus β and a distinct axial force-displacement hysteresis (normalized using the average axial strain). Unlike higher-mode buckling and friction effects, which occur at a specific compressive *force*, the binding force started to increase at a specific compressive *displacement*. Furthermore, the increase in compressive force was independent of the core strength, depending primarily on the confining stiffness and strength of the restrainer and limited only by the restrainer's axial strength. Figure 16 depicts the effect of the CHS restrainer's hoop tension action for W3A-10m-B, which experienced compressive forces (P_c = −3366 kN) of over three times the core's yield strength, or about 50% of the restrainer's squash load. Note that these post-binding forces should be treated as rough estimates, as the confined mortar strength and debonding gap depend on volumetric expansion of the mortar, which was intentionally underestimated, while migration of the crushed mortar grains was not modeled, which may delay binding in subsequent cycles.

If core binding occurs, β may be sensitive to otherwise insignificant changes (e.g., mortar age, mix and dynamic stiffness; restrainer shape and breadth-to-thickness ratio). These nuanced property and detail variations would be difficult to adequately capture in a limited testing program and could plausibly result in β > 1.5, the limit prescribed by AISC 341-16,[6] even if β was acceptable for the qualification test specimen. Conversely, a strong restrainer and small debonding gap are needed to prevent restrainer bulging,[4] and so a conservative design to minimize the post-binding force is unconservative in terms of the bulging resistance. Given the uncertainty and consequences for global stability, a preferred approach is to prohibit core binding during qualification tests, regardless of whether β complies with the design standard, and then to prevent core binding through design. This may be achieved by explicitly designing the strong axis debonding gap (s_s) for the expected compressive strain amplification associated with β_F.

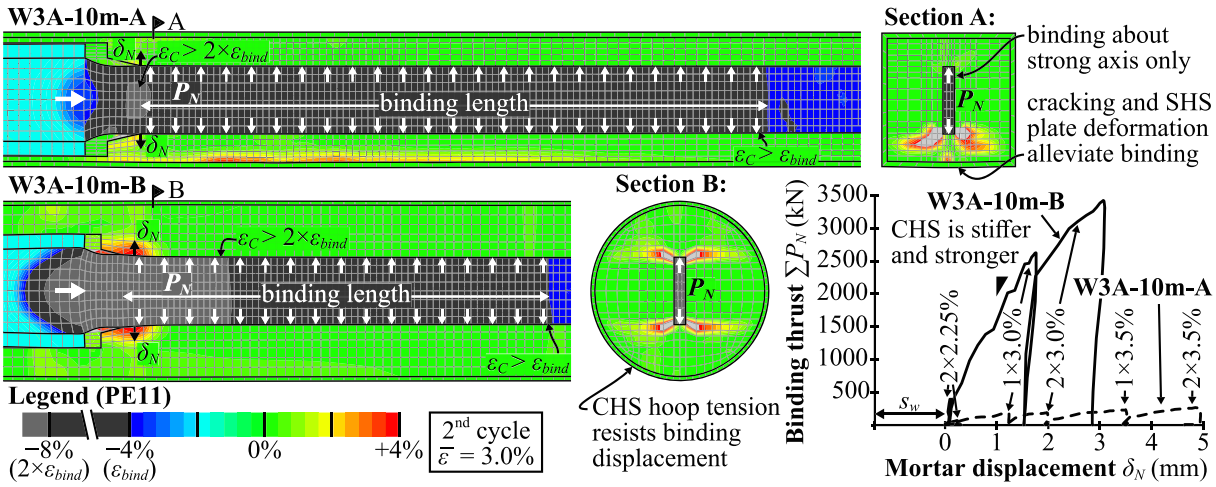

FIGURE 16 Friction-induced core binding

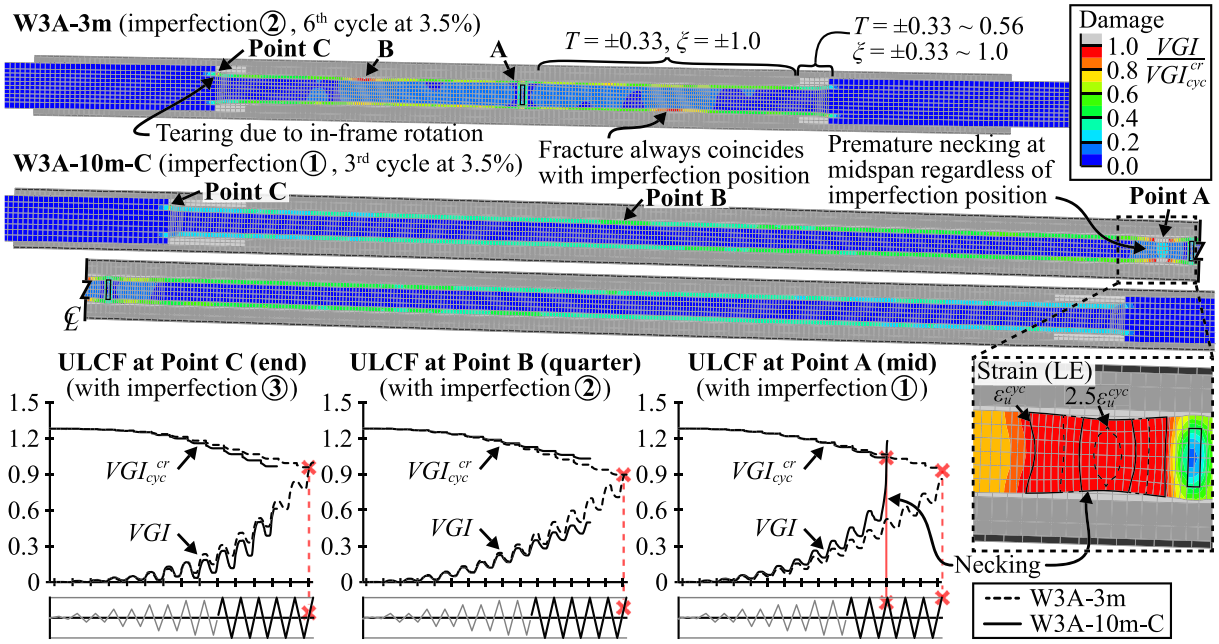

FIGURE 17 Ultra low cycle fatigue (ULCF) damage and fracture

6.2 | Fatigue and fracture

A larger strong axis debonding gap was adopted for W3A-10m-C, increasing the critical binding strain to ε_{bind} = 9%. Equation 13 indicates that this will accommodate $\beta \approx 1.19$ at $\bar{\varepsilon}$ = 3.5% (i.e., β_F = 1.11), slightly exceeding the expected overstrength scaled from W3A-3m. The numerical model reached β = 1.14 at $\bar{\varepsilon}$ = 2.25% and β = 1.20 at $\bar{\varepsilon}$ = 3.5%, increasing slightly to β = 1.23 during the final fatigue cycle. Although core binding was effectively eliminated, the fatigue capacity was reached at the start of the third rather than sixth cycle at $\bar{\varepsilon}$ = 3.5%. The ULCF damage evolution is shown in Figure 17 for the W3A-3m and W3A-10m-C models with imperfections located at positions ①, ②, or ③.

The fatigue damage along the yield length of W3A-3m indicated fracture during the sixth tensile cycle at $\bar{\varepsilon}$ = 3.5% with *CID* = 850, which is nearly identical to the experimental result of *CID* = 880. The fracture location always coincided with the modeled imperfection position (①, ②, or ③), but position ② is shown in Figure 17, as this is where fracture occurred in the experiment. Although fracture was also indicated in the same cycle at the core end corners due to the subassemblage rotations, this region had an enlarged cross section and only minor tearing was observed in the experiment at these locations.[8]

Conversely, W3A-10m-C always fractured near midspan after necking, regardless of the imperfection position and subassemblage rotation. For imperfection position ③, fracture was indicated at the start of the third cycle at $\bar{\varepsilon}$ = 3.5% with *CID* = 560 (35% reduction from W3A-3m), which is similar to previous experimental observations.[7,9] However, the compounding effects of $\bar{\varepsilon}$ and β_F on cyclic strain ratcheting (e.g., Equation 7, Figure 5b and Figure 10c) increased the tensile strains in a highly nonlinear manner, such that fracture was almost entirely driven by the three peak cycles. Therefore, a purely ascending loading protocol where fracture occurs in one of the first few peak cycles may not give a good indication of the fatigue capacity of long BRBs, as the peak cycles often occur early in real earthquake ground motions. Due to the increased sensitivity to the peak amplitude, it may be prudent to adopt a lower design strain in long BRBs to ensure a safety margin against premature necking during the first few peak cycles.

7 | ANALYTICAL PROPOSAL

The previous sections suggest that an accurate estimate of β_F is required to successfully design long BRBs, as β_F affects the strain amplitudes ε_C and ε_T, which determine the strong axis debonding gap and design strain, respectfully. This section proposes an analytical estimate of β_F and strain design criteria.

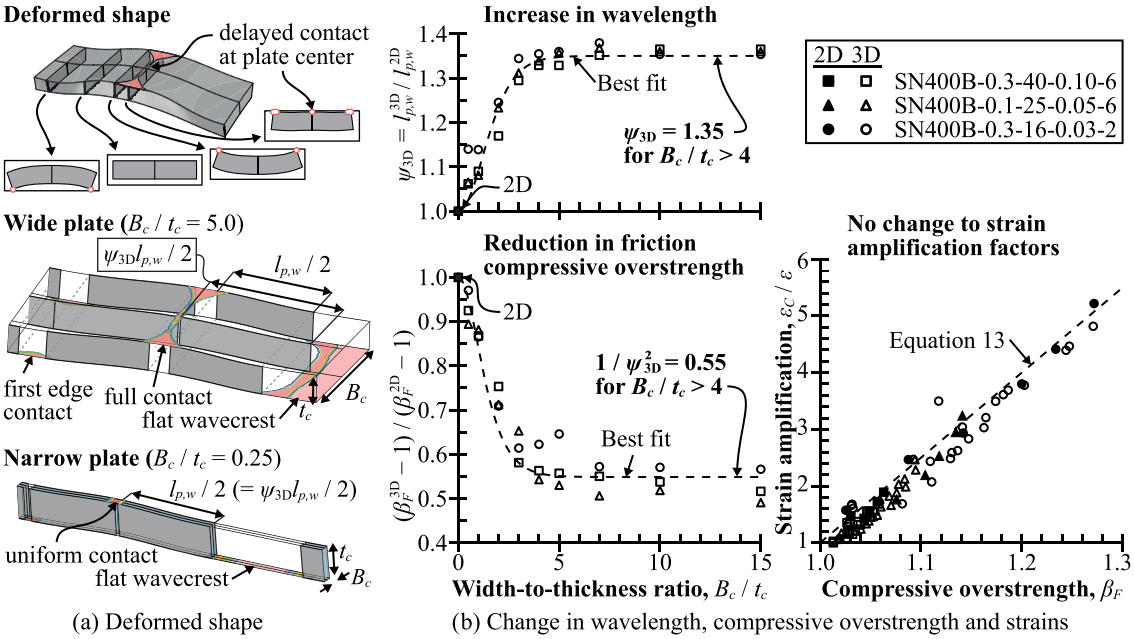

FIGURE 18 Effect of plate width and contact sequence

7.1 | Higher-mode buckling wavelength

First, the plastic higher-mode buckling wavelength is required, which from Section 3.2 consists of a flat wavecrest length and sinusoidal bending segments. However, the sinusoidal bending segments are further lengthened in wide plates due to the anticlastic shape of inelastic plate deformation,[28] which causes the edges to come into contact first (Figure 18a).[17] The edges then act as concentrated supports until the middle of the plate deflects enough to make contact, during which the corresponding edge deflections expand the edge contact length. Given that the plate edge wavelength is at least equal to the 2D case, the wavelength along the centerline increases by the ratio between the middle and edge contact positions, which is denoted the 3D plate contact factor (ψ_{3D}).

On average, a 3D plate contact factor of ψ_{3D} = 1.35 was confirmed for wide core plates (B_c/t_c > 5) by analyzing a set of 3D models with different B_c/t_c ratios (modeled as per Figure 14 but constrained to weak axis buckling only and with the restrainers replaced by analytical rigid surfaces) (Figure 18b). This agrees with the normalized weak axis wavelengths ($\psi_W l_{p,w}/t_c$ = 10–12) observed after bulging experiments, which tend to be about 40% longer than those in the strong axis ($\psi_W l_{p,s}/B_c$ = 7–8).[4] On average, 70% of the lateral thrust was concentrated over the middle 80% of the plate, and β_F decreased by ψ_{3D} squared (i.e., $\beta_{F,3D} = 1 + (\beta_{F,2D} - 1)/\psi_{3D}^2$), while the axial strain amplification factors remained unchanged for a given β_F (Figure 18b).

Therefore, the weak ($l_{p,w}$) and strong ($l_{p,s}$) axis wavelengths (Equations 17a and 17b) may be calculated from the cyclic stress–strain curve with k_e = 2.0 and $E_{eff} = E_t$, while only applying the 3D plate contact factor (ψ_{3D} = 1.35) to $l_{p,w}$. The full wavelength randomly varies, and is greater than $l_{p,w}$ and $l_{p,s}$ by ψ_W = 1.34, on average. For the adopted constitutive material model, the true stress $\bar{\sigma}$ when cycled at $\pm\bar{\varepsilon}$ (i.e., at the balance point) is given by Equation 18 and the corresponding tangent stiffness $\bar{E}$ by Equation 19, where $\bar{\varepsilon}_p$ is the average plastic strain and $\sum\bar{\varepsilon}_p$ the average cumulative plastic strain obtained from the axial loading protocol.

$$l_{p,w} = \psi_{3D} \cdot t_c \cdot 2\pi\sqrt{\frac{\bar{E}_t}{3\bar{\sigma}}} \tag{17a}$$

$$l_{p,s} = B_c \cdot 2\pi\sqrt{\frac{\bar{E}_t}{3\bar{\sigma}}} \tag{17b}$$

$$\bar{\sigma} = \sigma_0 + Q_\infty\left(1 - e^{-b\cdot\sum\bar{\varepsilon}_p}\right) + \sum_{i=1}^{3}\frac{C_i}{\gamma_i}\cdot\tanh(\gamma_i\bar{\varepsilon}_p) \tag{18}$$

$$\bar{E}_t = \frac{d\bar{\sigma}}{d\bar{\varepsilon}^{pl}} = Q_\infty b e^{-b \cdot \sum \bar{\varepsilon}_p} + \sum_{i=1}^{3} C_i (1 - \tanh(\gamma_i \bar{\varepsilon}_p)) \tag{19}$$

7.2 | Compressive overstrength factor

An analytical closed-form estimate of the friction compressive overstrength factor (β_F) may then be obtained using the empirical overstrength-to-friction force ratio of ρ = 0.55 (Equation 12). Assuming that weak axis higher-mode buckling dominates and thrust is linearly distributed along the core, the average individual wavecrest friction (F_i) (Equation 20) may be determined from the two adjacent weak-axis half-wavelengths ($0.5l_{p,w}$) (Equation 17a), compressive force ($\beta_P P_T$) and waveheight ($2s_w - 0.5\bar{\varepsilon} \cdot t_c$) at the balance point.

$$F_i = \mu \cdot \beta_P P_T \cdot 2(2s_w - 0.5 \cdot \bar{\varepsilon} \cdot t)/0.5l_{p,w} \tag{20}$$

Assuming a midspan shear key ($L_F = L_p/2$) and wavecrest length factor of ψ_W = 1.34 (Figure 6c), there are $N = L_F/(0.5\psi_W l_{p,w})$ wavecrests along the friction length. The friction compressive overstrength factor β_F is then given by Equation 21. Note that narrow plates (B_c/t_c < 5) would also need to include the strong axis contribution and adopt a smaller plate factor (ψ_{3D} < 1.35), and so there may be diminishing returns to increasing the core thickness if it results in a compact section.

$$\beta_F = 1 + \rho \frac{N \cdot F_i}{\beta_P P_T} \approx 1 + 0.55 \cdot \mu \cdot \frac{L_p}{\psi_W l_{p,w}} \frac{8s_w - 2 \cdot |\bar{\varepsilon}| \cdot t_c}{l_{p,w}} \tag{21}$$

Assuming the higher-mode buckling amplitude is small (e.g., s_w/t_c < 0.1) and no core binding, the compressive overstrength factor equals $\beta = \beta_P \beta_F$, where $\beta_P \approx 1 + 2\bar{\varepsilon}$ was introduced in Equation 3.

7.3 | Validation

Figure 19a compares the proposed analytical method (Equations 17a–21, with ψ_W = 1.34) to the LY225∼SA700 results from Section 3, adopting ψ_{3D} = 1.0 as these are 2D models. The error in the quantity ($\beta_F - 1$) was within −10%/+20%, which corresponds to an error in β of −2%/+4%. It may be noted that given a known s_w and μ, the previous closed-form proposals[7,11] overestimate ($\beta_F - 1$) by an additional $1/(\rho\psi_W)$ = +35%, as they assume that the cumulative friction is directly additive (i.e., $|P_C| = \beta_F P_T + F$, or ρ = 1.0), but calculate lateral thrust using the full wavelength ($\psi_W l_{p,w}$). Therefore, the proposal offers superior accuracy than the existing closed-form proposals, given a known friction coefficient and debonding gap, while providing a more realistic estimate of the restrainer force.

Next, the proposed method (using SN490B, ψ_W = 1.34 and ψ_{3D} = 1.35) was compared (Figure 19b) to Dehghani's method[14] for the 96 models listed in Table 3, retaining the original 350WT material model and setting $\xi = 1/\gamma = 2\psi_W$ = 2.7. This numerical method requires the

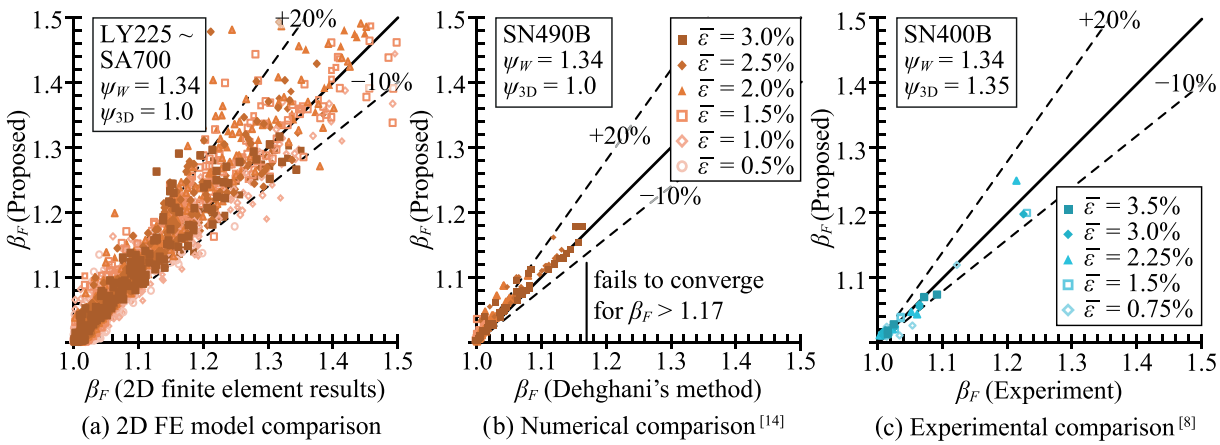

FIGURE 19 Validation of analytical estimate of β_F

stress and effective stiffness at each wave, but in practice, the real hysteresis is only symmetric at the balance point and permanent tensile strains may occur at midspan, even without strain ratcheting. Consequently, the originally proposed (symmetric) material model[14] did not converge for $\beta_F > 1.17$. Nevertheless, good agreement was obtained over the limited range where a solution was obtained using Dehghani's method.

Finally, the proposed method (using SN400B, $\psi_W = 1.34$ and $\psi_{3D} = 1.35$) was compared (Figure 19c) to a set of experimental results (WPSC1, 1A, 2, 3, 3A, and 4 from Terashima[8]). A pressure–velocity-wear friction model for one-way sliding and a 50 MPa mortar countersurface was employed where μ varied from 0.25 to 0.09 with increasing contact pressure, assuming a contact area of $t_c \times B_c$. Detailed calculations may be found in the dissertation of the first author. Once again, the proposed method was in good agreement.

This brief validation indicates that the proposed method offers reasonable accuracy for large β_F values, overcomes the limitations of previous proposals, and if $l_{p,w}$ is precomputed, is amenable to hand calculation.

7.4 | Peak axial strain check

After calculating β_F, the peak axial strains may be determined from the applied average axial strain ($\bar{\varepsilon}$) and empirical amplification factors ($\varepsilon_C/\bar{\varepsilon}$ and $\varepsilon_T/\bar{\varepsilon}$) from Section 4. While strictly only valid for the symmetric, increasing protocol in Figure 3c and material models in Table 2, the empirical amplification factors offer a good first estimate of whether friction-induced binding or premature necking may be a problem. Note that they do not include bending strains associated with higher-mode buckling, nor local strain concentration.

The compressive strain (ε_C) at the core end may be obtained from Equation 13, which gives $\varepsilon_C/\bar{\varepsilon}$ as a function of β_F. Although in principal ε_C should have a safety factor against the critical binding strain (ε_{bind}) (Equation 15), a strain capacity reduction factor of $\phi_C = 1.0$ is suggested, as Equation 15 has some built-in conservatism. If unsatisfactory, a slightly larger strong axis debonding gap (s_s) may be provided, accompanied by a restrainer bulging check.[4]

$$\varepsilon_C = \frac{\varepsilon_C}{\bar{\varepsilon}} \cdot \bar{\varepsilon} < \phi_C \varepsilon_{bind} \tag{22}$$

Similarly, the tensile strain (ε_T) at midspan may be estimated from Equation 14, which gives $\varepsilon_T/\bar{\varepsilon}$ as a function of $\bar{\varepsilon}$ and β_F at the second peak cycle of an ascending protocol. Note that ε_T rapidly increases with $\bar{\varepsilon}$ due to the compounding effects of $\bar{\varepsilon}$ and β_F on cyclic strain ratcheting, and so should be kept well below the cyclic ultimate strain ε_u^{cyc}. Therefore, a strain capacity reduction factor of $\phi_T = 0.6$ is suggested (e.g., $\phi_T \varepsilon_u^{cyc} = 0.6 \times 16\% = 10\%$ for SN400B). If unsatisfactory, the BRB core size may be increased to reduce the design strain, or the core configuration revised to reduce the slenderness and β_F.

$$\varepsilon_T = \frac{\varepsilon_T}{\bar{\varepsilon}} \cdot \bar{\varepsilon} < \phi_T \varepsilon_u^{cyc} \tag{23}$$

The safe design strains from Equations 22 and 23 are shown in Figure 20 for LY100∼SA440B. This indicates that core binding is usually critical for long BRBs, although premature necking may still be a concern for $\bar{\varepsilon} > 2$–3% and $\beta_F > 1.2$, depending on the steel grade. Finally, fatigue is a function of the local stress state, amplified axial strains, bending strains and imperfections, and so the precise reduction in *CID* for long BRBs depends on the specific detailing. Therefore, Equation 23 should only be considered as an upper bound limit, and a safety margin included when assessing compliance with code fatigue provisions.

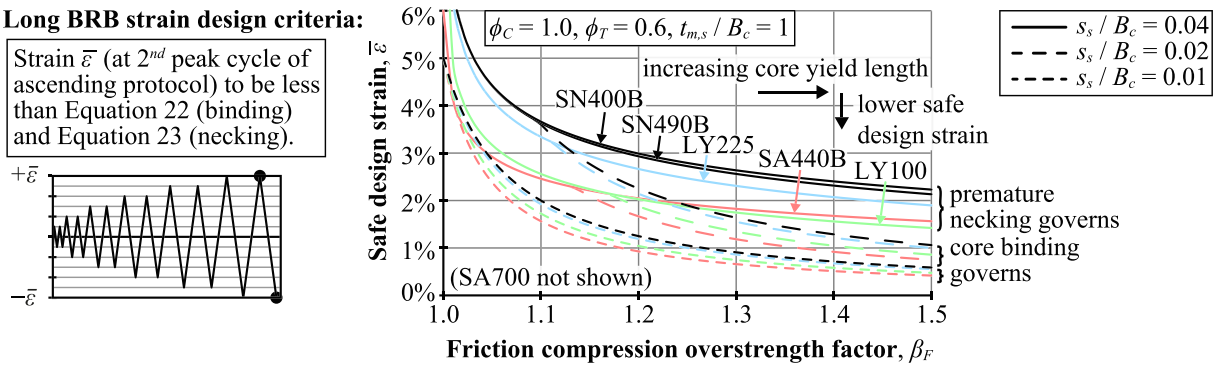

FIGURE 20 Safe design strain

7.5 | Implications for global stability

Although Equation 22 should prevent a disastrous increase in force due to core binding, long BRBs will still be subjected to larger compressive overstrength forces than shorter BRBs, which must be considered in the global stability analysis. Also, the fundamental assumption of a negligible restrainer axial force is not valid when β_F is large, as Section 4.1 found that the restrainer axial force is almost twice the increase in compressive force (i.e., restrainer force = $F = \beta_P P_T (\beta_F - 1)/\rho$, where $\rho \approx 55\%$). This is particularly important given that AISC 341-16 now permits β values up to 1.5.[6] Additionally, increasing the compressive force and effective length may require large, heavy restrainers that attract substantial gravity and inertial forces, which the global stability analysis must account for. This gives a clear imperative to minimizing friction in long BRBs.

8 | CONCLUSIONS

A parametric numerical modeling approach was employed to investigate the effects of higher-mode buckling and friction in long, rectangular core BRBs with low yield (LY100, LY225), conventional (SN400B, SN490B) and high strength (SA440B, SA700) steel grades. The amplified axial strains in long BRBs with slender cores, which have seen limited testing to date, were found to introduce undesirable phenomena that are not observed in short BRBs, nor prevented by AISC 341-16.[6]

- Friction compressive overstrength (β_F) was proportional to μ, s_w, L_p, and $1/t_c^2$, but the uncertainty in the wavecrest length introduced a standard deviation of ±0.02. Steel grade also affected β_F, which was minimized for SN400B and SN490B, with the quantity ($\beta_F - 1$) increased by +20–50% for both significantly lower (LY225, LY100) and higher (SA440, SA700) steel grades.
- Compressive strains (ε_C) at the core ends increased linearly with β_F and the average axial strain ($\bar{\varepsilon}$). Core binding occurred in long BRBs with small strong axis debonding gaps, resulting in large compressive forces that were sensitive to minor detailing changes.
- Tensile strains (ε_T) at midspan increased linearly with β_F, but nonlinearly with $\bar{\varepsilon}$ due to cyclic strain ratcheting. Premature necking was found to be the primary cause of the low fatigue capacities observed in long BRBs, as β_F had a minor effect on the local cumulative strain demand.
- Equations were proposed to estimate β_F, ε_C and ε_T, providing a robust method to select the debonding gap and design strain in long BRBs, and evaluate the feasibility of slender core designs.

In summary, axial strain amplification is an important side effect of compressive overstrength. The proposed equations may prove useful when designing long BRBs, or if full-scale testing is not feasible.

ORCID

Ben Sitler https://orcid.org/0000-0001-5551-9879
Toru Takeuchi https://orcid.org/0000-0001-7430-4734

REFERENCES

[1] L. Joseph, K. Gulec, J. Schwaiger, *Int. J. High-Rise Build.* **2016**, *5*, 1.
[2] I. Almufti, J. Krolicki, A. Crowther, *Struct. Mag.* **2016**, *5*, 42.
[3] Y. L. Guo, P. Zhou, M. Z. Wang, Y. L. Pi, M. A. Bradford, J. Z. Tong, *Eng. Struct.* **2017**, *148*, 157.
[4] T. Takeuchi, A. Wada, *Buckling-restrained braces and applications*, JSSI, Tokyo **2017**.
[5] H. Gong, X. Wang, D. Hu, X. Guo, *Bldg. Struct.* **2013**, *6*, 32. (in Chinese)
[6] AISC, *Seismic provisions for structural steel buildings*, AISC 341–16, **2016**.
[7] K. C. Tsai, A. C. Wu, C. Y. Wei, P. C. Lin, M. C. Chuang, Y. J. Yu, *Earthq. Eng. Struct. Dyn.* **2014**, *43*, 1785.
[8] M. Terashima, Ductile fracture simulation and risk quantification of buckling-restrained braces under earthquakes, PhD Thesis, Stanford University, **2018**.
[9] P.W. Richards, B. Saxey, NZSEE annual tech. Conf., Wellington, New Zealand **2017**.
[10] H. Yoshikawa, K. Nishimoto, H. Konishi, A. Watanabe, Nippon steel tech. Report 10–01, **2010**. (in Japanese)
[11] M. Midorikawa, M. Iwata, T. Wakayama, R. Iizuka, T. Okazaki, T. Asari, 10th U.S. Natl. Conf. Earthq. Eng., Anchorage, Alaska **2014**.
[12] M. Midorikawa, T. Wakayama, T. Asari, M. Iwata, *J. Struct. Eng., AIJ* **2014**, *60B*, 307. (in Japanese)
[13] Q. Chen, C. L. Wang, S. Meng, B. Zeng, *Eng. Struct.* **2016**, *111*, 478.
[14] M. Dehghani, R. Tremblay, *J. Constr. Steel Res.* **2017**, *138*, 608.
[15] V. Budaházy, L. Dunai, *J. Constr. Steel Res.* **2015**, *115*, 92.
[16] A. C. Wu, P. C. Lin, K. C. Tsai, *Earthq. Eng. Struct. Dyn.* **2014**, *43*, 375.
[17] G. Metelli, G. Bregoli, F. Genna, *J. Constr. Steel Res.* **2016**, *122*, 409.
[18] M. Smith, *ABAQUS/Explicit User's Manual*, version 2017, Simulia, **2017**.
[19] K. Kasai, K. Nishizawa, AIJ annual meeting, Toyama, Japan **2010**, 807. (in Japanese)
[20] Nippon Steel, *Construction materials handbook*, Nippon Steel Corp., Tokyo **2019**. (in Japanese)
[21] T. Ono, A. Sato, *J. Struct. Constr. Eng. (Trans. AIJ)* **2000**, *532*, 177. (in Japanese)

[22] M. Wang, L. Fahnestock, F. Qian, W. Yang, *Construct. Build Mater.* **2017**, *131*, 696.
[23] H. Yamazaki, K. Kasai, Y. Ono, H. Kaneko, K. Sadasue, AIJ annual meeting, Yokohama, Japan **2006**, 935. (in Japanese)
[24] J. L. Chaboche, *Intl. J. Plast.* **1989**, *5*, 247.
[25] F. Genna, G. Bregoli, *J. Mech. Mater. Struct.* **2014**, *9*, 441.
[26] N. H. Nguyen, A. S. Whittaker, *Eng. Struct.* **2017**, *150*, 1.
[27] C. Smith, G. Deierlein, A. Kanvinde, Blume center tech. Report TR-187, Stanford University, **2014**.
[28] S. Timoshenko, S. Woinowsky-Krieger, *Theory of plates and shells*, McGraw-Hill, New York **1959**.

How to cite this article: Sitler B, Takeuchi T. Higher-mode buckling and friction in long and large-scale buckling-restrained braces. *Struct Design Tall Spec Build*. 2021;30:e1812. https://doi.org/10.1002/tal.1812